buildings

MDPI

Article

Design and Verification of a Novel Structural Strain Measuring Method Based on Template Matching and Microscopic Vision

Chenhao Zhao [1,2], Bingchuan Bai [1,2], Lianyue Liang [1,2], Ziyu Cheng [1,2], Xixian Chen [1,2], Weijie Li [1,2,*] and Xuefeng Zhao [1,2,*]

[1] School of Civil Engineering, Dalian University of Technology, Dalian 116024, China; zhaochenhao@mail.dlut.edu.cn (C.Z.); tstark@mail.dlut.edu.cn (B.B.); lianglianyue@mail.dlut.edu.cn (L.L.); chengziyu@mail.dlut.edu.cn (Z.C.); 11906018@mail.dlut.edu.cn (X.C.)

[2] State Key Laboratory of Coastal and Offshore Engineering, Dalian University of Technology, Dalian 116024, China

* Correspondence: liweijie@dlut.edu.cn (W.L.); zhaoxf@dlut.edu.cn (X.Z.)

Abstract: Strain measurements have a significant role in evaluating the condition of various structural types and have become an essential component in the area of structural health monitoring. However, there are some limitations in the current means of strain measurement, and this study aims to improve these methods. We have designed a novel strain measurement method based on template matching algorithms and microscopic vision techniques, developed a new sliding strain sensor, and paired it with a new microscope to realize strain measurement. The method has the function of remote wireless acquisition with a cell phone, which is more widely applicable. In the laboratory performance testing, the zero drift of the sensor is mainly concentrated in the fluctuation range of ± 2 $\mu\varepsilon$, and the effective range reaches nearly 40,000 $\mu\varepsilon$. In the comparison experiments with the linear variable differential transformer, the maximum error of the static loading is only 5 $\mu\varepsilon$, and the maximum error rate of the dynamic loading is less than 1%, which proves that it has a relatively high accuracy. Finally, the short-term real-time monitoring of the local structure of the footbridge was accomplished, and the strain changes on the surface of the structure were captured instantly, stably, and efficiently in the actual measurements. The proposed strain measurement system has the advantages of high accuracy, a low cost, convenient measurement, and wide applicability, and it provides a novel alternative means for strain measurement in the field of structural health monitoring.

Keywords: strain measurement method; sliding strain sensor; template matching; microscopic vision; structural health monitoring; design and validation

check for updates

Citation: Zhao, C.; Bai, B.; Liang, L.; Cheng, Z.; Chen, X.; Li, W.; Zhao, X. Design and Verification of a Novel Structural Strain Measuring Method Based on Template Matching and Microscopic Vision. *Buildings* **2023**, *13*, 2395. https://doi.org/10.3390/buildings13092395

Academic Editor: Humberto Varum

Received: 23 August 2023
Revised: 14 September 2023
Accepted: 19 September 2023
Published: 21 September 2023

1. Introduction

Civil structures and infrastructures, such as buildings, airframes, wind turbines, tunnels, and bridges, occupy an important place in the economy and play a vital role in improving the standard of living of the world's population. These structures are experiencing premature damage and may reach the end of their lifespan sooner than expected [1]. Ensuring life safety and reducing inspection costs have become top priorities for engineers and researchers in recent decades. Automating the condition assessment process of civil structures is the only practicable solution for the efficient management of aging infrastructure networks. This task can be pursued by structural health monitoring (SHM) systems that link the experimental observation (e.g., by sensors) of the in-service response of a structure to its structural integrity (e.g., damage diagnosis and health prognosis) [2]. As a data processing method, SHM employs techniques to provide early signals of disruption and damage progression in order to avoid potentially hazardous outcomes for a given structure [3]. Moreover, the establishment of a proper monitoring system can effectively reduce the cost of necessary measures, such as structural inspection and maintenance [4]. Therefore, many platforms have emphasized the importance of cost-effective SHM to ensure long-term structural integrity and safety levels [5–8]. Current SHM mainly includes tasks such as displacement monitoring [9,10], damage detection and assessment [11,12], strain monitoring [13], and local structural identification [14], where structure-specific strain monitoring plays a crucial role in assessing the condition of various structure types [15–19]. The strain data measured against a structure can be used to assess the structural properties, failure behavior, crack extension, and residual stresses in the stressed components of the structure [20–22]. Therefore, strain monitoring has become an integral part of the SHM field.

In order to effectively monitor the stresses and strains imposed on structural components, researchers have worked on developing a variety of strain sensors that employ different sensing mechanisms. These include resistance strain gauges [23], fiber optic sensors [24], and vibrating wire strain gauges [25]. Although these sensors are well known for their excellent accuracy and stability and have been widely used in important structures, such as bridges [26–28], tunnels [29], and high-rise buildings [30,31], they have certain problems in practical strain measurement applications in the field. For example, conventional strain gauges are limited in their ability to realize large-area sensing due to their limited size and time-consuming and laborious surface preparation process. In addition to this, they require periodic calibration to collect an accurate response, and they are very sensitive and can be damaged by overloading and/or extreme temperatures [32]. Vibrating wire strain gauges, while robust, are difficult to replace in the event of failure because they need to be embedded in concrete for measurements. They also need to be used in conjunction with data acquisition equipment, and complex preparation and wiring procedures limit their application to common structures. Fiber Bragg grating strain sensors are widely used for strain measurement in different disciplines [33–36]. They have the advantages of a light weight, non-conductivity, and resistance to electromagnetic noise, but they are prone to zero drift. They show vulnerability during long-term measurements and need to be paired with a costly demodulator, which is also not favorable for wide-range strain measurements. Distributed fiber-optic sensors have good prospects for measuring strain distribution as well as concrete crack detection. However, they have not yet been widely used in practice due to their overly complex installation process, low installation survival rate, and over-reliance on the professional interpretation of measurement results [37].

The improvement of camera pixel technology has led to the rapid development of optical measurement techniques based on image processing, which promotes the application of non-destructive testing techniques. The main representative is digital image correlation (DIC) technology, which has significant advantages, such as non-contact, non-destructive, and full-field measurement [38,39]. However, the accuracy is often low due to the influence of measurement equipment, image noise, and algorithms. Meanwhile, the high cost of measurement equipment limits its application in practical measurement. In contrast, with the development of calculator vision technology, machine vision-based strain measurement methods are popular due to their accuracy and independence from light [40–42]. In addition, vision-based methods offer advantages in terms of installation and speed compared to conventional DIC techniques. Some results have been achieved in industrial production and SHM [43–47].

On the basis of our previous research, a micrograph strain sensing method based on machine vision algorithms has been introduced for strain measurements using cellular phones. Sleeve-type strain sensors have been designed [48–51], and the possibility of replacing a cell phone with a digital microscope for long-term monitoring has been explored [52], and these studies have been subjected to preliminary laboratory validation. The system demonstrated the advantages of machine vision-based strain measurement due to its low cost, ease of measurement operation, and high accuracy. However, since the production of the sensors relies on manual labor, the production process lacks standardization and is susceptible to interference; at the same time, the selected microscope has limited functionality and relies on a circle detection algorithm that is sensitive to image quality, so the stability of the measurements is challenged when encountering variations in lighting conditions and shooting angles, and these problems will hinder the application of the sensors for real-world measurements. Therefore, the main objective of this study is to improve the existing strain measurement means based on previous research to address the problems of a high cost, complicated operation, and over-reliance on specialized personnel.

The major contribution of this research is the successful development of a more convenient strain measurement system based on the template matching algorithm and microscope vision techniques. The new multifunctional microscope employed for the sensors has the function of remote wireless acquisition via a cell phone, which has a wider scope of application. In the meantime, on-site monitoring does not need to be coupled with specialized instruments. The cost is relatively low, the operation is more convenient, even non-professionals can be quickly engaged in the strain measurement work, and it is universally applicable to the structure. In particular, short-term on-site measurements of the local structure of the footbridge were completed, and the performance of the sensor was tested in practice. In conclusion, this study has designed and validated a high-precision, low-cost, convenient, and widely applicable structural strain measurement method that provides a novel and universally applicable alternative means of strain measurement in the field of SHM.

This paper is organized as follows: At first, the strain measurement system developed in this research is described, including an overview of the sensors, the computational principles, and the algorithms used. Then, the results of the laboratory performance tests of the sensors and the comparison experiments with a linear variable differential transformer (LVDT) are presented, and the results are discussed to analyze the performance of the sensors. In addition, the results of strain measurements on a real structure are presented to further demonstrate the actual measurement performance of the sensor. Finally, the whole paper is summarized.

2. Strain Measurement System

The strain measurement system is mainly composed of two parts, hardware and software, where the hardware mainly includes sliding strain sensors, a new multifunctional microscope, data transmission lines, and cell phones or laptops, while the software will mainly introduce the principle of the method to calculate strain and the algorithms used in this method.

2.1. Sensor Overview

The overall structure of the new sliding sensor is shown in Figure 1, which includes four main parts: a sliding measurement device, a vision module, an adjustable clamping mechanism, and a multifunctional microscope. The sliding measurement device is bolted and fixed to the measurement points on the surface of the structure to be measured by two supports (shown as support 1 and support 2 in Figure 2), which are used to capture the strain changes at the measurement points. The vision module (shown as a red rectangle in Figure 1) consists of two photolithographic targets located at the vision platform (shown as a yellow area in Figure 2) of the sliding measurement device, and the strain information captured by the sliding measurement mechanism will be transmitted to the vision module. The information changes in the vision module are then captured by the new multifunctional microscope above, where the multifunctional microscope can be adjusted to a specified angle and fixed to the sliding measurement mechanism by means of an adjustable clamping device. Ultimately, the information collected by the microscope is calculated using an algorithm to obtain the final strain data. Each part of the sensor structure is described in detail below, and the measurement procedure, efficiency, and production cost of the sensor are given at the end.

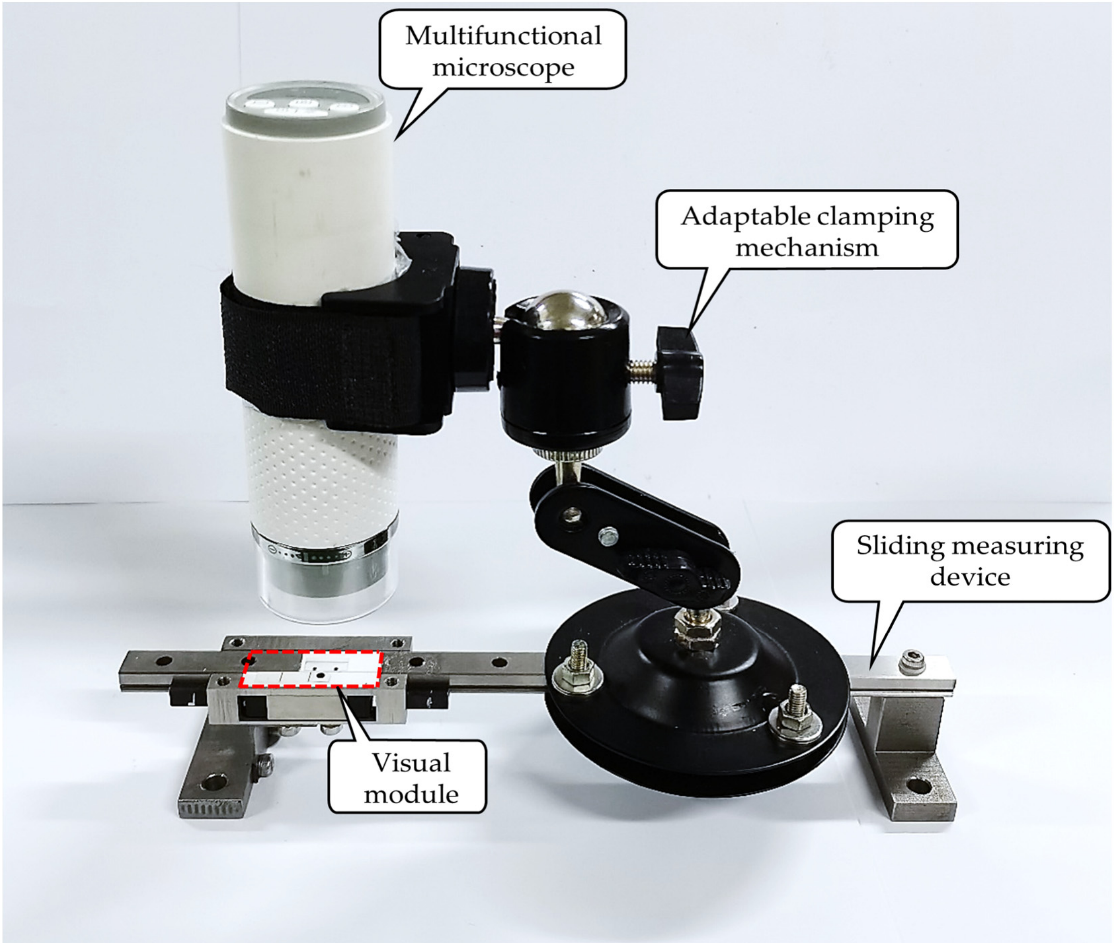

Figure 1. The general structure of the sensor.

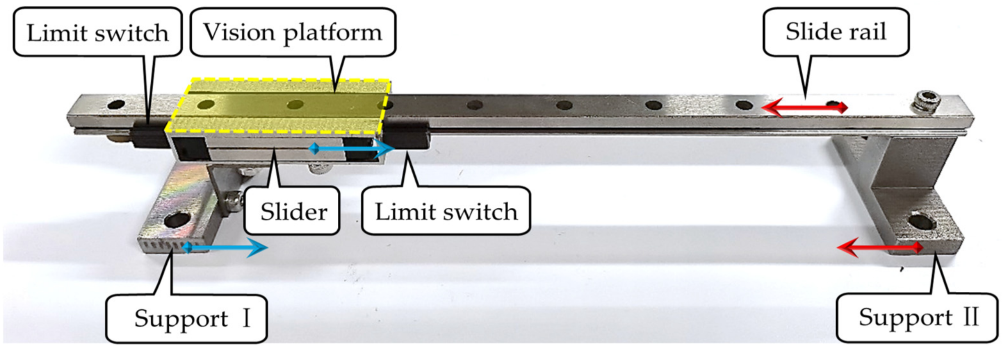

Figure 2. Physical drawing of the sliding measuring device.

2.1.1. Sliding Measurement Device

The slide measurement device is made of stainless steel and consists of a slide rail, a slider, two limit blocks, and two supports, as shown in Figure 2. The slider is mounted under the slide rail, with internal ball bearings designed to move smoothly along the slide rail. At the same time, the height of the slider and the upper surface of the slide rail are the same, forming a horizontal vision platform (yellow rectangular area in Figure 2) for the installation of the vision module. The through holes are reserved at an equal spacing in the center of the slide rail, and four bolt holes are left at the bottom of the slider to provide convenient installation of the support. In addition, the length of the slide can be adjusted according to the measurement requirements of the target structure to meet the different spacing requirements of strain measurement. The sensor is provided with two supports:

support 1 is bolted to the bottom of the slider, support 2 is bolted to the end of the slide rail, and the bottom of the support is designed with bolt holes for the installation and fixation of the sensor measurement. The limiting device is mounted on both sides of the slider, and the braking of the slider is realized by adjusting the tightness of the screws, thus realizing the control of the sensor switch. When structural strain measurement is carried out, two supports are fixed at two measuring points on the surface of the structure, and the distance between the measuring points is the measuring distance of the sensor. When the structure generates strain, the standoffs undergo a corresponding movement, which is then equivalently transferred to the relative movement between the slider and the slider at the vision platform (as shown by the blue and red arrows in Figure 2), and ultimately the structural strain capture is realized by recording the relative displacement pattern occurring in the vision module.

2.1.2. Vision Module

The vision module consists of two targets mounted on the vision platform, whose identifiers are black circles printed by thin-film lithography with micrometer accuracy, as shown in Figure 3. Target 1 (the blue area in Figure 3) contains a solid circle with a radius of 1 mm, and Target 2 (the red area in Figure 3) contains two solid circles with a radius of 0. 5 mm, and their centroid distance is 5 mm. In this case, Target 1 is fixed on the surface of the slider at the vision platform and responds to the displacement change of support 1 (shown by the blue arrow in Figure 3), while Target 2 is fixed on the surface of the slide rail at the vision platform and responds to the displacement change of support 2 (shown by the red arrow in Figure 3). Since the vision platform is close to horizontal, theoretically the two targets are located in the same plane, thus ensuring that the multifunctional microscope achieves the best observation effect, and ultimately the strain change on the surface of the structure will be reflected as the relative displacement change between the two targets.

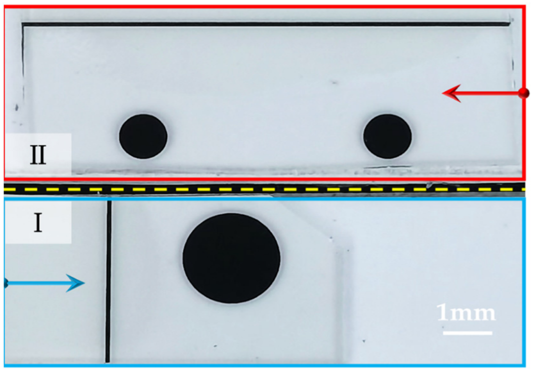

Figure 3. The physical picture of the vision module.

2.1.3. Adjustable Clamping Device

As shown in Figure 4, the adjustable clamping device is assembled from four components. At the bottom is a magnetic support that can be fixed directly to the surface of the slider rail, and, for a more stable fixation, a disc-shaped clamping device was further developed that can be bolted tightly to the slider rail (as shown in Figure 1). Attached to the bottom is a leveling mechanism for adjusting the length of the stretch, and the tension adjustment knob is fixed after determining the angle. The top is fitted with a universal ball joint that can be rotated in any direction and is fixed with a knob after the angle has been determined. Finally, attached to the ball joint is a microscope mounting clip that holds the microscope firmly in place. This adjustable clamping device can accurately adjust the position and observation angle of the microscope according to the measurement requirements and fix it firmly on the slide rail, making the fixing and adjustment of the microscope more stable and convenient.

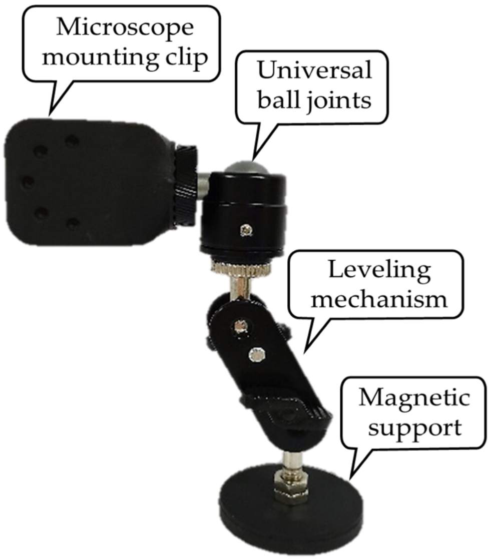

Figure 4. The physical picture of the adjustable clamping device.

2.1.4. Multifunctional Microscope Overview

This sensing uses a new multifunctional WIFI microscope as shown in Figure 5, and its detailed parameters are shown in Table 1. Its multifunctionality is highlighted in that it supports both USB connection to the computer and direct remote connection to the cell phone through the WIFI hotspot, which improves the convenience and diversity of measurements. The remote connection function with a smartphone is suitable for short-term spot-check inspections of structures, while the computer connection is ideal for the long-term stable monitoring of structures, and this versatility is more favorable for structural measurements in complex environments. In addition, the microscope has the functions of taking pictures, video recording, and file storage. There is a circle of fill light designed at the mouth of the mirror, and the intensity of the fill light is graded and adjustable so that it can fully avoid the influence of different external lighting environments on the measurement. It is more suitable for the application of micro-vision technology, and it can make timely and accurate records of changes in the displacement information generated by the vision module.

Figure 5. The physical picture of the multifunctional microscope.

Table 1. Detailed parameters of the multifunctional microscope.

Parameter Type	Parameter Information
Pixel	5 million pixels
Magnification	50–1000×
Photo resolution	1920 ∗ 1080 P
Video resolution	1280 ∗ 720 P
Focus distance	Manual focus (2–60 mm)
WIFI connection distance	10 m (open condition)
Photo format	JPG
Video Format	MP4/AVI
Dynamic frame rate	20–30 f/s
System compatibility	Android 6.0+, iOS 9.0+, Windows 7–11, Mac OS X 11.0+
Battery Capacity	800 MA

2.1.5. Sensor Usage, Efficiency, and Production Costs

The sensor can be used as follows: First, before the measurement, the sensor is assembled and connected to a cell phone or computer. Then, after the locations of the measurement points on the surface of the structure to be measured are determined, the sensor can be installed by fixing the two supports to the two measurement points, respectively. Then, the relative positions of the measurement points are used to determine the measurement distance of the sensor, and a microscope is used to record the information of the vision module when the sensor is not unlocked, i.e., the initial displacement of the sensor is recorded. Finally, the limit device of the sensor is opened to start the strain measurement.

From the above measurement steps, it is easy to realize that the sensor had been debugged before the measurement. In use, it is only necessary to adjust the measurement distance according to the measurement point, install and fix the support, and then immediately carry out strain measurement after connecting to the computer or cell phone. The sensor is highly efficient because it eliminates the need for cumbersome wiring and instrument commissioning. At the same time, because the new microscope selected by the sensor has multifunctionality when regular strain spot-check inspection tasks are required, with a cell phone for remote wireless acquisition, the measurement work is more efficient and convenient; when long-term monitoring tasks need to be carried out, the computer can be used wired to collect the data in a way that ensures the stability of the strain measurement. The high adaptability of this sensor makes it more widely used and more efficient for measurement.

The main cost of the sensor comes from the production of the sliding measuring device and the purchase of the multifunctional microscope. The market price of a single microscope is about USD 30. Due to the standardized production parameters of the sliding measurement device and its mature processing, the production cost is less than USD 20. In summary, the total cost of the sensor is about USD 50, which is relatively low.

2.2. Principle and Algorithm

In the previous section, the structure of each part of the sensor and the use of the method were introduced. It is not difficult to find that the core of the sensor's ability to effectively capture the structural strain information lies in the accuracy of the microscope's recording of the visual module information, and the core of the strain calculation depends on the algorithm's processing ability. The following is an introduction to the principles of computation and algorithms used in this measurement method.

2.2.1. Calculation Principle

This method uses three circles in the micro-image as a recognition tool. The detection of circular objects in digital images is an important and recurring problem in image processing and computer vision [53]. This study selects the circular target as the recognition object based on the advantages that it is easier to find the center of the circle compared to other complex shapes, the algorithmic recognition effect is relatively better, and the production of the target is relatively easy.

Figure 6a shows the picture of the target taken by the microscope; the large circle selected in blue is from Target 1, and the two circles selected in red are from Target 2. We know that the two small circles are relatively static, and when the strain changes, the large circle will move relative to the two small circles. The main principle of the calculation is to accurately capture the changes in the coordinates of the three circles through the algorithm and calculate the relative displacement of the large circle relative to the two small circles through the change in the coordinates of the center of the circle, so as to obtain the relative displacement L between the two targets and ultimately calculate the strain size.

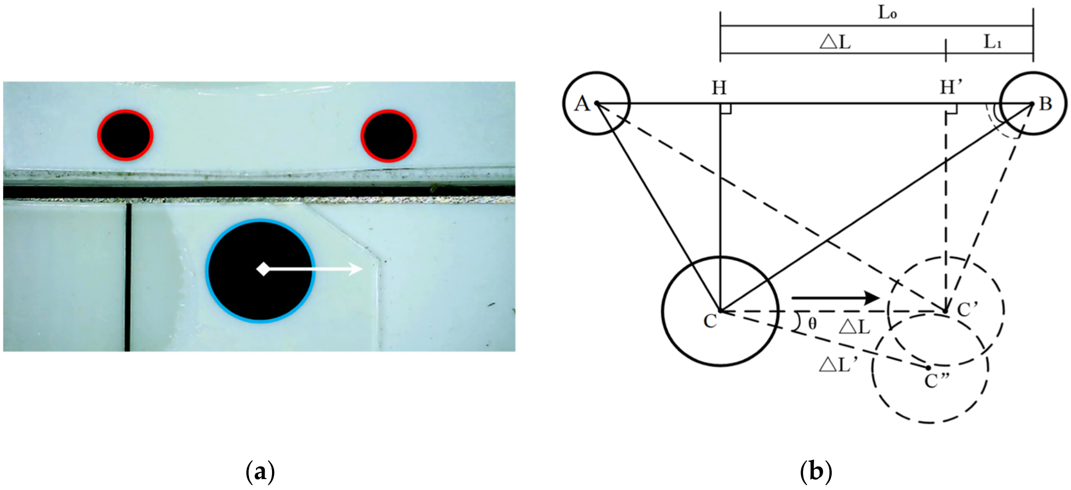

Figure 6. Physical picture of the vision module and the corresponding schematic of the calculation principle: (**a**) image of the vision module acquired through a microscope; (**b**) schematic diagram of the calculation principle.

Figure 6b shows the main calculation process, in which the three circles correspond to the three circular targets in the target. A, B, and C represent the centers of the three circles, and the coordinates of the centers can be accurately determined by the algorithm. In the ideal case, the moving trajectory of the large circle is noted as CC'. Theoretically, CC' is parallel to AB, so L can be calculated by calculating the length of the line segment CC'. The specific calculation process is as follows:

$$\because AB_{||}CC', CH\perp AB, C'H'\perp AB$$

Suppose that

$$BH = L_0, BH' = L_1$$

$$\therefore \Delta L = CC' = HH' = BH' - BH = L_1 - L_0 \quad (1)$$

In ΔABC :

$$BH = BC \times cosb$$

$$cosb = \frac{|AB|^2 + |BC|^2 - |CA|^2}{2 \times |AB| \times |BC|} \quad (2)$$

The relative displacement ΔL can be obtained from Equation (1), and the center coordinates of the circle are known. The lengths of AB, BC, and AC can be calculated according to the distance formula, and then the value can be calculated using the cosine theorem, as shown in Equation (2), i.e., if the center coordinates of the circle of the three points of ABC are known, the length of L can be found out, and the difference between the different L and L_0 can be found out.

However, due to inherent uncertainties during target fabrication, absolute parallelism between the two small circle centerlines AB and the larger circle's trajectory CC' cannot be ensured. In practice, a slight angle θ surfaces between CC' and AB, as illustrated in Figure 7. Consequently, the practical relative displacement adopts the following form:

$$\Delta L' = \Delta L \times cosb \quad (3)$$

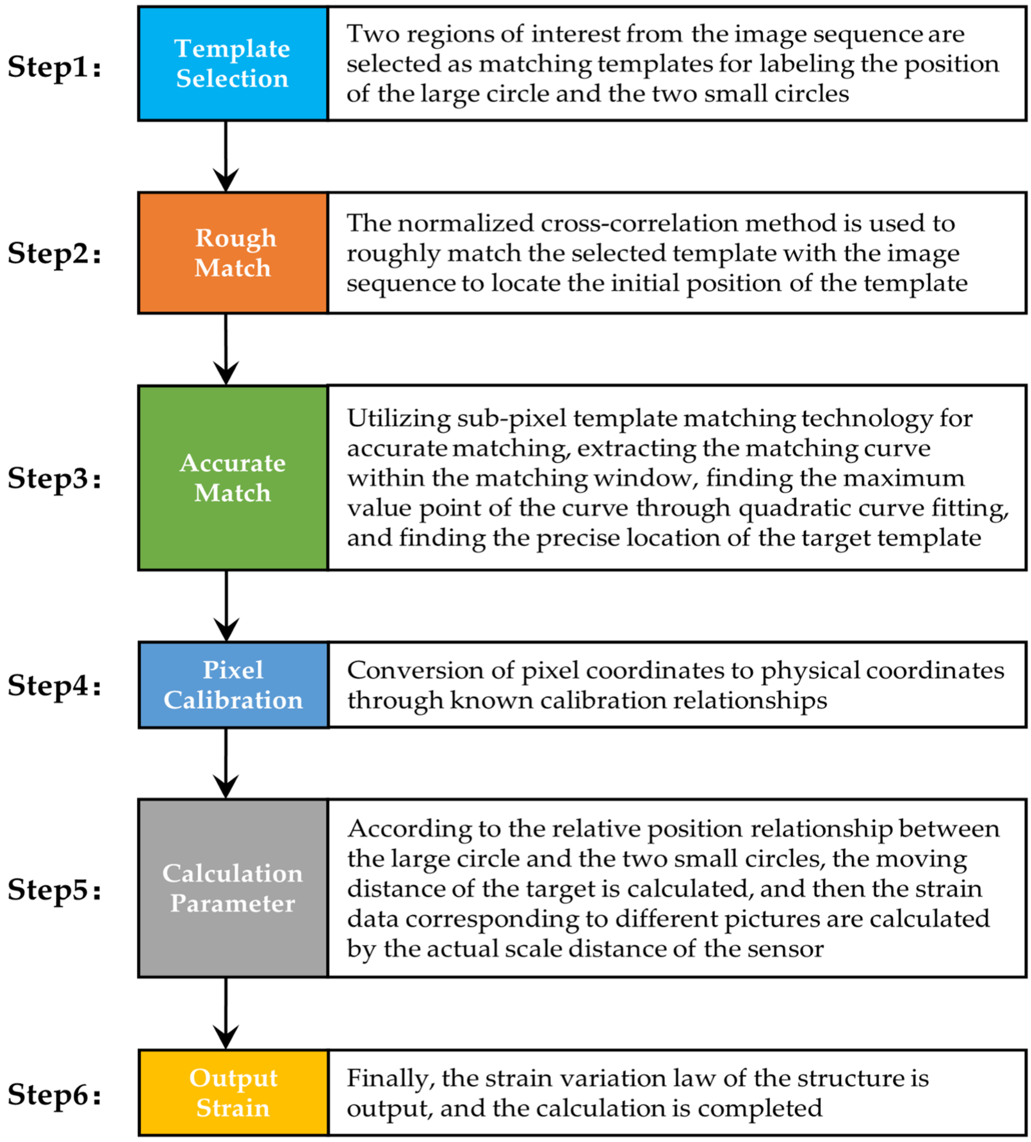

Figure 7. Schematic depiction of the algorithm's calculation process.

In order to make the calculation accurate, a pre-experimental correction is carried out: under the premise of reducing other disturbing factors, the sensor is loaded at full scale, the pictures of the initial position and the end position are recorded, and the algorithm is used to accurately identify the position of each center of the circle in the initial and end states:

$$A(x_a, y_a), B(x_b,\ y_b), C(x_c,\ y_c); A(x_{a'},\ y_{a'}), B(x_{b'},\ y_{b'}), C(x_{c'},\ y_{c'})$$

$$k_{AB} = \frac{x_b - x_a}{y_b - y_a}, k_{CC'} = \frac{x_{c'} - x_c}{y_{c'} - y_c} \quad (4)$$

$$tan\theta = \left| \frac{k_{AB} - k_{CC'}}{1 + k_{AB}k_{CC'}} \right| \tag{5}$$

$$cos\theta = \sqrt{\frac{1}{1 + tan^2\theta}} \tag{6}$$

Using Equation (4) to find the slopes of the lines AB and CC', calculate the cosine of the angle θ from Equations (5) and (6).

To summarize, the initial displacement L_0 is obtained by calculating the data image at the initial moment of the sensor, then a series of L_1 at different moments in the data image are calculated, and the difference between the different L_1 and L_0 is calculated to arrive at the displacement change L' at each moment. Since the scale distance of the sensor is known to be L, the final displacement change L' is calculated by Equation (7).

$$\varepsilon = \frac{\Delta L'}{L} \tag{7}$$

2.2.2. Template Matching Algorithm

It is obvious from the introduction of the principle that the accuracy of strain calculation mainly depends on the accuracy of the algorithm in recognizing and locating the target object. In this study, we use the template matching algorithm. Template matching is the process of determining the position of a pattern or template in an image according to specific criteria. It is one of the most commonly used techniques in signal and image processing [54] and is widely used in many fields related to computer vision and image processing, such as defect detection [55], image recognition [56], image alignment [57], and image inspection [58].

It is worth mentioning that an ideal circle detection algorithm should be able to operate with a fixed set of internal parameters across all images, i.e., without the need to tune the parameters for different images, be very fast; be able to detect multiple sizes of circles; be able to deal with synthesized, natural, and noisy images; have a high detection rate and good accuracy; and be able to produce few or no false detections. The circle detection algorithms proposed in the current research have several problems; for example, the most classical circle detection algorithm based on Hough's circle transform [59] is slow, has a high memory requirement, and is prone to producing many false detections. The improved CHT-based algorithm [60] has improved in terms of computational accuracy, but it still consumes a lot of memory and is slow in real-time applications. In addition, although other optimized circle detection algorithms have been proposed [61,62], they still cannot solve the constraints between computational accuracy and efficiency better. In practical applications, we note that most circle detection algorithms require high-quality circular targets; particularly, in the presence of noise the circumference of the circle often becomes less clear, which reduces the recognition quality of the algorithm. The existence of these problems limits the feasibility of current circle detection algorithms in practical applications, especially in complex environments where accurate measurements need to be made in real time in scenarios where current circle detection algorithms are clearly less applicable.

In contrast, the template matching algorithm chosen in this study is more suitable for scenarios requiring real-time computation due to its simpler structure, higher computational efficiency, and stable recognition. It is more effective in recognizing and matching fixed-size targets, and the clever design of the sensor has avoided changes in the lighting environment and shooting angle as much as possible, thus weakening the sensitivity of the algorithm to rotation, scaling, and lighting conditions. In addition, in sub-pixel template matching, various interpolation techniques or curve fitting methods are used to achieve sub-pixel accuracy matching, and the accuracy of the algorithm can fully meet the measurement requirements. For comprehensive consideration, the template matching algorithm is selected for target identification and localization, and the algorithm is developed for the target used in this study. The main calculation process of the program is shown in Figure 7. The algorithm can achieve sub-pixel-level calculation accuracy, show better identification and localization effects, and ensure the accuracy of strain calculation.

3. Laboratory Performance Evaluation

3.1. Experimental Details

In order to verify the accuracy of this strain measurement method, we conducted experimental tests for the new slide-type strain sensor and focused on various parameter indicators of the sensor, including zero drift, range, repeatability, stability, accuracy, and static and dynamic measurement performance. The experimental setup includes an optical platform, a control platform, a counterweight block, a sensor, a cell phone, a computer, a control loading instrument, and a data acquisition instrument. The experimental arrangement and the corresponding equipment are shown in Figure 8. Equally spaced bolt holes are provided on the optical platform to provide a precision mounting platform for the experiment. The control platform involved in the experiment consists of a fixed platform mounted on the optical platform and a moving platform connected to the stepper motor. Both platforms have the same height and are equipped with equally spaced bolt holes for mounting fixed sensors.

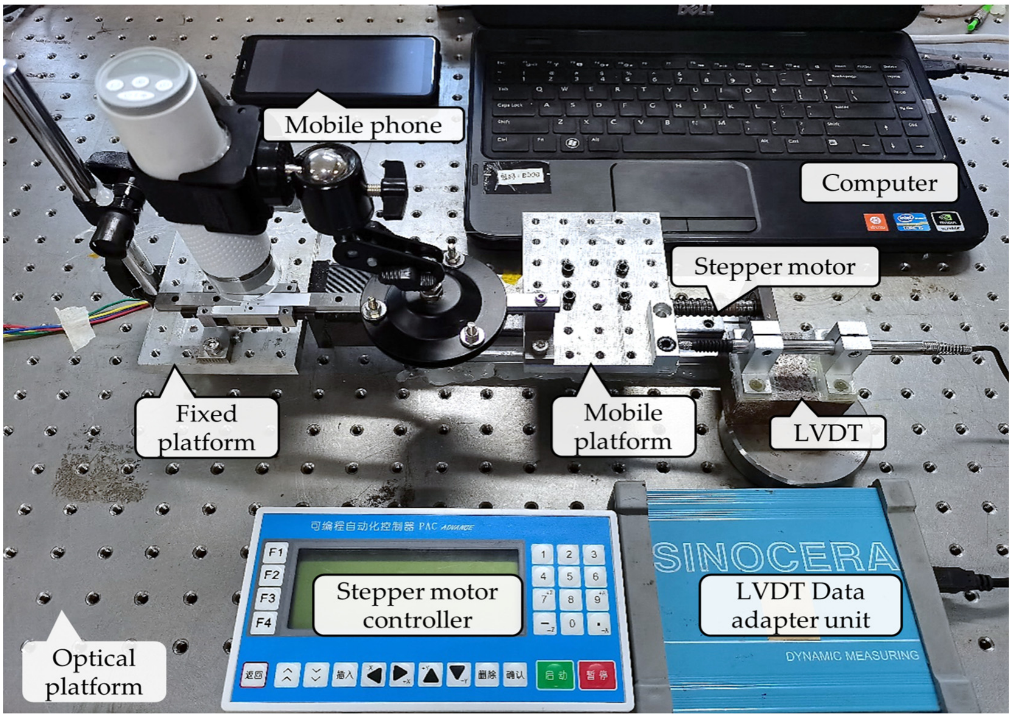

Figure 8. Schematic diagram of experimental setup.

A single-axis stepping motor was chosen for the loading device of this experiment, which was mounted on the optical platform and used to control the movement of the moving platform along the axial direction to realize the loading of the working conditions. When the experimental loading task is executed, the stepper motor controller needs to input the corresponding commands according to the specified conditions. The loading conditions in this experiment mainly involve static loading and unloading at equal distances, as well as dynamic loading by applying periodic reciprocating motion at a fixed speed. The detailed conditions are specified in the corresponding tests below. The two supports of the sensor are mounted on the two control platforms by bolts; the left support remains stationary on the fixed platform, and the right support is mounted on the moving platform of the stepping motor and follows the moving platform. It can be seen that this experiment is to realize the loading of different working conditions by way of a stepping motor controlling the right support of the sensor to move along the sensor axis relative to the left support. The LVDT was chosen for the experimental comparison device, and its data were acquired through a data acquisition unit. The LVDT is placed on the right side of the moving platform in the experiment, and the accurate displacement measurement is realized by ensuring that it is parallel to the axis of movement of the stepping motor. Since the LVDT is a robust absolute linear displacement sensor with high measurement accuracy and a sufficient measurement frequency, the measurement accuracy of this sensor can be effectively demonstrated.

The sensor scale distance used in the experiment is 150 mm, and the angle correction value is 0.9996. For the convenience of the experiment, we chose the microscope with a wired connection to the computer for data acquisition, and, whether you use a cell phone for remote wireless measurement or a computer for wired connection measurement, only the applicable measurement object and the environment are not quite the same, so the actual measurement of the accuracy does not have an impact. The following section describes the specific experimental process of each performance test in turn then describes the process of static and dynamic comparison experiments and analyzes the experimental results.

3.2. Performance Testing

3.2.1. Zero Drift

The size of zero drift is mainly affected by many factors, such as ambient temperature, pressure, humidity, light, the sensor production, the acquisition method, the stability of the algorithm, etc. If the value of zero drift is too large, it may cause the signal output from the sensor to deviate from the true value, affecting the accuracy and reliability of the measurement. Therefore, in order to test the zero-drift performance of this sensor in the static state, we chose to collect data from the sensor for up to 10 min in the laboratory without external load input, using the two recording modes of taking pictures and recording videos for the two acquisition modes of remote cell phone acquisition and wired computer acquisition, respectively.

As shown in Figure 9, the strain value of the sensor under remote acquisition via cell phone varies in the range of ±3 με, in which the zero drift in both photo and video modes mainly focuses on the fluctuation in the range of ±2 με. As shown in Figure 10, the strain value of the sensor under wired computer acquisition varies within the range of ±2 με, in which the zero drift mainly focuses on the fluctuation within the range of ±1 με in both photo and video modes.

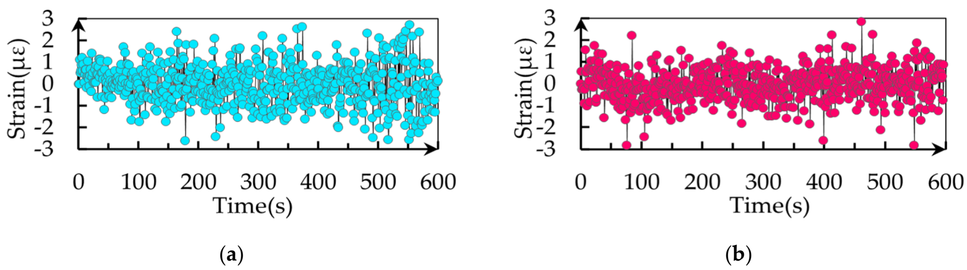

Figure 9. Zero drift data collected remotely via cell phone: (**a**) photographic mode; (**b**) video mode.

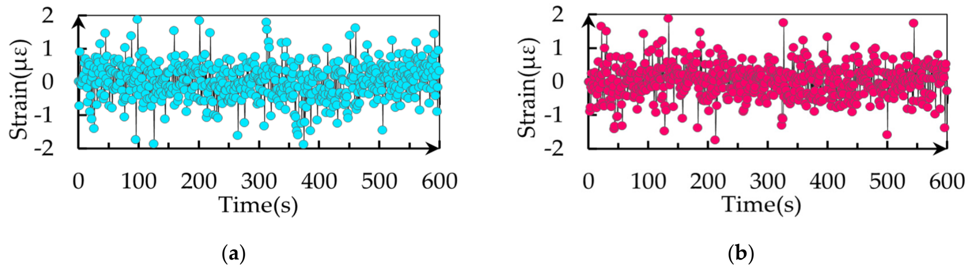

Figure 10. Zero drift data collected through wired computer acquisition: (**a**) photographic mode; (**b**) video mode.

In comparison, the zero-drift fluctuation of the wired computer acquisition is smaller than that of the remote cell phone acquisition, which is because the stability of the wired control acquisition is better. At the same time, it is easy to see from the figure that for both acquisition modes the data recorded with the camera recording mode will be relatively volatile compared to the data recorded with the photo mode. This is because the camera recording mode is more continuous and less prone to perturbation, while the photo mode requires a single photo recording each time the microscope is controlled, which is relatively more perturbing.

Among the main causes of data fluctuation, regardless of which mode is used, is the error in the detection of the matching process by the template matching algorithm. Although the fluctuation patterns of the data recorded by the two shooting modes corresponding to the two acquisition methods are slightly different, they all meet the requirement of mainly focusing on the fluctuation in the range of ±2 με, and the data as a whole basically conform to the normal distribution, which proves that the zero drift of the sensors is relatively small and the measurement process is relatively stable.

3.2.2. Measurement Range

The range of the sensor is mainly determined by the size of the target, the field of view of the microscope, the algorithm of recognition, and the limitations of the sensor's mechanical structure. The microscope used in this sensor has a function of manual focusing, and the change in focal length will affect the size of the observation field of view, so the observation equipment has the ability to increase the range to a certain extent compared with the fixed-focus microscope, and, at the same time, the aberration around the field of view of the microscope is small, which is beneficial to the assurance of the range. In order to accurately test the actual measuring range of the sensor, we used a stepper motor to load the sensor at full scale at 200 microns per step to test the effective observed range of the sensor.

The results of the full-scale experiment are shown in Figure 11, and we observe that the effective measuring range of the sensor can reach 39,490 με, so the effective tensile range of the sensor can be considered to be ±19,745 με. It is worth noting that, because the observing field of view and the target can be adjusted, the range of the sensor can actually be expanded; however, the current range is already sufficient to meet the needs of various types of actual engineering structural strain measurements.

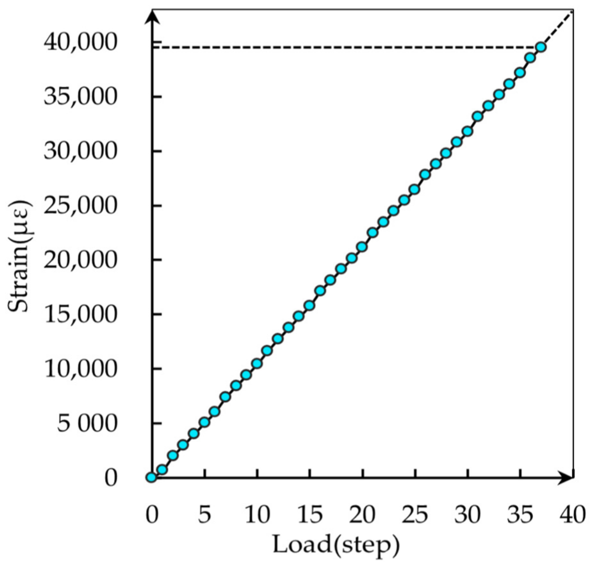

Figure 11. Experimental data from the full-scale experiment.

3.2.3. Reproducibility Assessment

The repeatability of a sensor refers to the degree of difference between the output values obtained from repeated measurements under the same measurement conditions, which directly affects the accuracy and reliability of the measurement results. In order to evaluate the repeatability performance of the sensor, we used a stepper motor to carry out repeatability loading experiments. The single-step loading–unloading process was repeated more than 30 times for each set of experiments in steps of 10 μm and 20 μm, respectively, and the changes in the sensor data were recorded.

The experimental results are shown in Figure 12, in which the data after unloading are uniformly zeroed in order to more intuitively show the volatility of the repetitive experimental data, and the figure focuses only on the volatility of the strain measurements during the loading process. It is calculated that under a 10 μm loading condition the strain data of the repeatability experiment fluctuates from −0.099 με to 0.104 με, and the standard deviation of the measured data is 0.352 με under 30 loadings; under a 20 μm condition, the strain fluctuates from −0.607 με to 0.901 με, and the standard deviation of the data is 0.456 με. From the results, it can be found that the fluctuation of the strain data of the sensor under repeated loading in a single step under the working condition is very small, and, at the same time, the repeatability of the sensor is not affected by the different loading steps, which fully proves that the sensor has good repeatability, and the measurement results are stable and reliable.

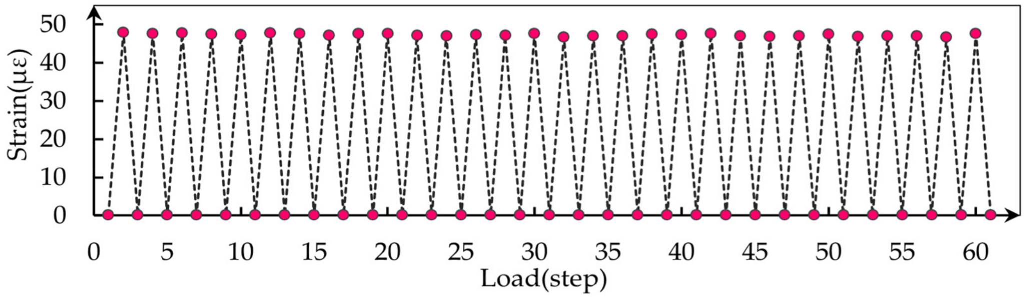

(**a**)

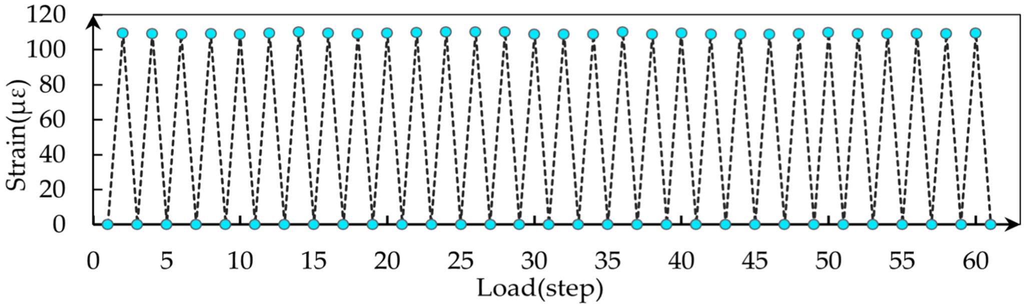

(**b**)

Figure 12. Experimental data from repetitive loading experiments: (**a**) 10 μm step; (**b**) 20 μm step.

3.3. Comparative Experiment: Static and Dynamic Evaluation

In order to observe the measurement performance of the developed sensor, this paper uses stepper motors to simulate the actual measurement process of the sensor via static and dynamic loading, respectively, and compares the data collected by the sensor and LVDT to further verify the stability and accuracy of the measurement process of the developed sensor.

3.3.1. Preloaded Experimental

In the experimental arrangement, we try our best to ensure that the sensor, LVDT, and stepper motor are on the same axis, but due to the existence of installation errors, there may be a certain angular difference between the sensor and the LVDT trajectory. This phenomenon will lead to a certain proportional error in the data of the two measurement methods under the same displacement loaded by the stepper motor. In order to eliminate the effect of the resulting error, we conducted a preloading experiment using a stepper motor for 5 μm equidistant loading for a total of 50 steps and measured by both means. The two pairs of data are compared to determine the scaling factor of the difference, which in turn is used to correct subsequent experiments involving comparisons.

As shown in Figure 13, the error of the two measurement methods increases linearly with the number of loading steps, which is caused by the fact that the sensor is not on the same axis as the LVDT. In order to correct this error, we compared the change rules of the two types of data in each loading step and obtained a correction factor of 1.01042. After correction, the maximum absolute error (MAXE) of the sensor measurement was only 2.44 με, and the mean absolute error (MAE) was only 0.916 με. The above results prove that the correction according to this correction coefficient can effectively eliminate the errors caused by the non-parallel axes of the sensor and the LVDT during the installation of the instrument. In the subsequent comparison experiments, the experimental data will be corrected according to this correction coefficient before comparison.

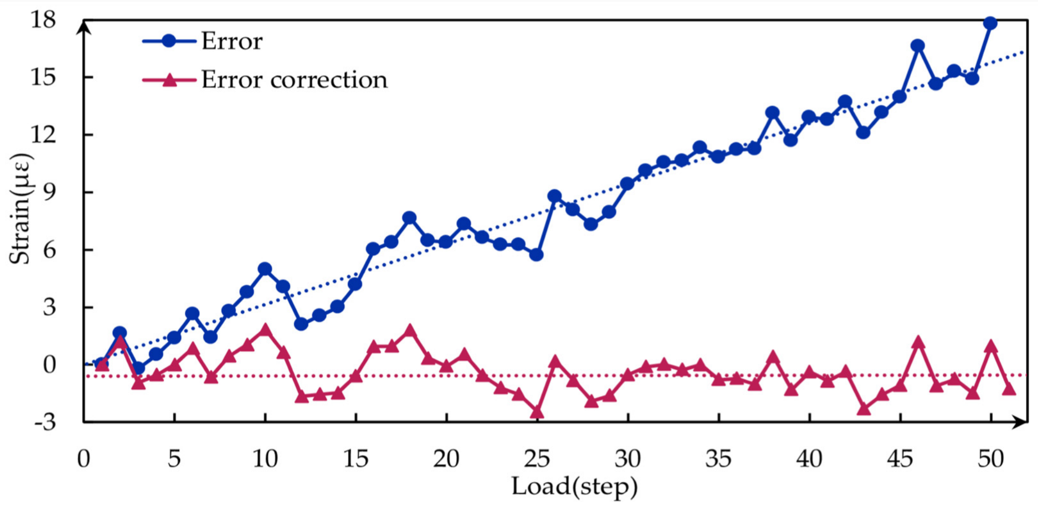

Figure 13. Original error data from preloading experiments and error data corrected using the correction factor.

3.3.2. Evaluation of Static Measurement Performance

In order to fully verify the static test performance of the sensor, we used a stepper motor to carry out 10 μm and 20 μm equidistant loading experiments. Each group of experiments loaded 10 steps, for a total of five groups of experiments. In each group of experiments, when loading is completed the stepper motor immediately returns to the initial position and continues to carry out the next group of experiments, so as to maintain the continuity of the loading process, the use of sensors and LVDT for continuous measurement, and the data obtained from the static loading comparison experiments.

From the data change rule, we found the phenomenon of unequal spacing between adjacent loading steps, which is due to the working principle of the stepper motor. Because we are more concerned about the results and errors of the comparison of the two means of measurement, this phenomenon has no effect on the results of the comparison experiment. From Figure 14a,b, it can be clearly observed that the strain data measured by the microscope combined with the sensor are in good agreement with the data measured by the LVDT, while the change in the sensor measurement error during the loading process has been obtained by calculating the difference between the sensor and the five sets of experimental data measured by the LVDT, as shown in Figure 14c,d, and the comparative data have been corrected. Compared with the LVDT, the MAXE of the strain data is 3.89 με and the MAE is 1.21 με for the 10 μm loading condition, and the MAXE of the data is 4.87 με and the MAE is 1.89 με for the 20 μm loading condition. The above results show that, in the five groups of comparative experiments conducted consecutively, the differences between the sensor measurement data and the LVDT measurement data are very small, and at the same time, the sensor measurement data of each group of experiments are relatively close to the LVDT measurement data. The groups of experimental measurement data are close to each other, which proves that the static measurement of the sensor under different loading conditions has high stability and accuracy and meets the requirements of strain measurement in SEM.

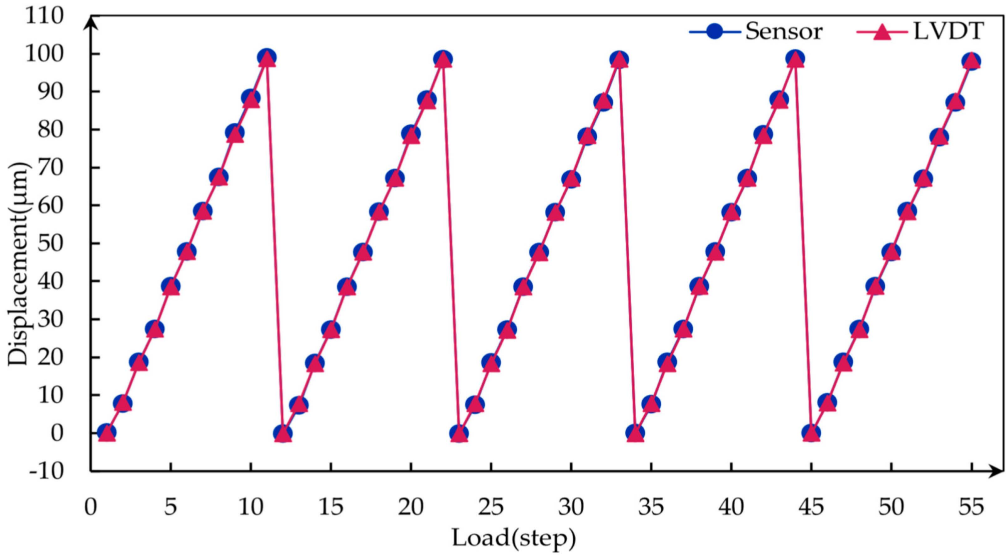

(**a**)

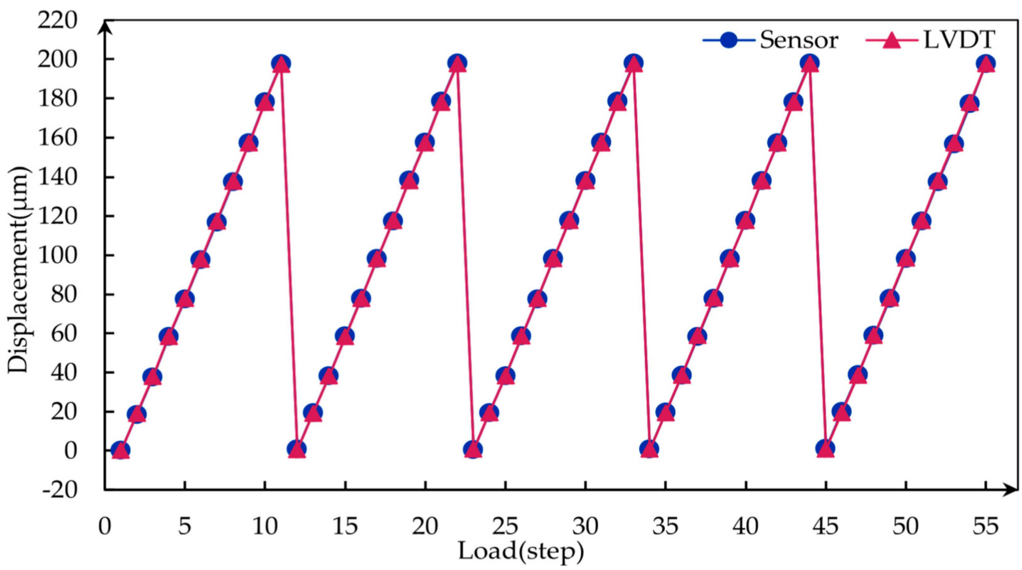

(**b**)

Figure 14. *Cont*.

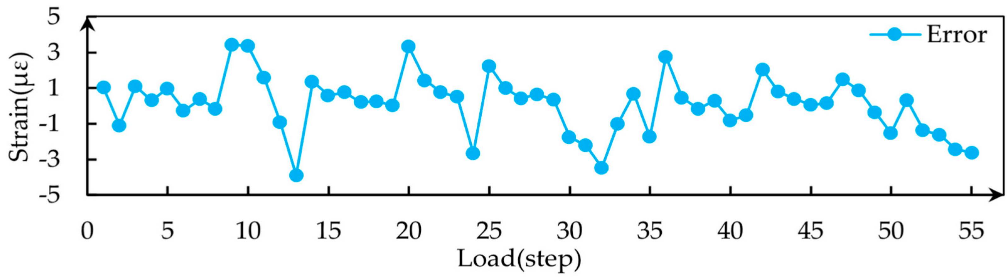

(**c**)

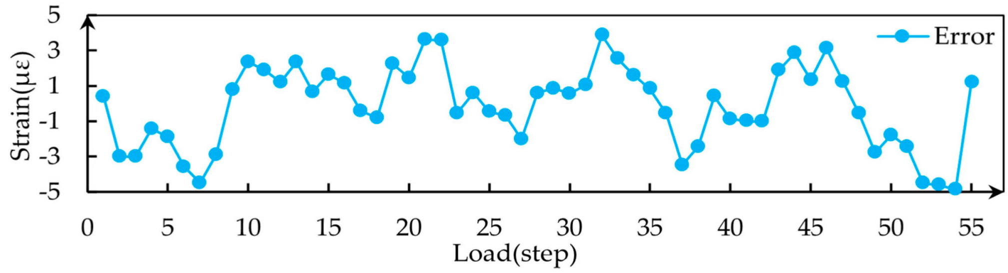

(**d**)

Figure 14. Experimental data and error data of static loading comparison experiments: (**a**) 10 μm loading experimental data; (**b**) 20 μm loading experimental data; (**c**) 10 μm loading error data; (**d**) 20 μm loading error data.

3.3.3. Evaluation of Dynamic Measurement Performance

In order to study the dynamic characteristics of the sensor, we use a stepper motor to simulate the reciprocating motion of the sensor and carry out dynamic reciprocating loading. The loading frequency is fixed at 30 Hz, and the peak value of loading is 200 μm. In the experiment, the sensor is acquired at a frequency of 30 Hz, and in order to ensure the validity of the comparison, the LVDT is acquired at a frequency of 50 Hz as a comparison.

The results of the data collected by the sensor and the LVDT are shown in Figure 15a, and the high degree of overlap between the two curves indicates that the dynamic acquisition of the sensor is in good agreement with that of the LVDT. This indicates that this sensor can accurately capture the dynamic strain response of the structure. It should be noted that the dynamic sampling frequency of the sensor is mainly limited by the frame rate of the video recorded by the microscope, except that the current sampling frequency of the sensor of 30 Hz is sufficient for the measurement of typical structures.

For the comparison of the dynamic peak data, we are mainly concerned with the peak error, so by subtracting the peak strain value obtained by the sensor from the corresponding peak value measured by the LVDT, the change in peak error between the two sensors is calculated as shown in Figure 15b. The corrected MAXE between the dynamically measured strain peak of the sensor and the LVDT strain peak is calculated to be 7.73 με, and the MAE is 3.68 με. The dynamic measurement of the sensor is performed using video segmentation, which results in a slight decrease in accuracy compared to the measurement method of taking high-pixel images in the static measurements. This is mainly due to the higher frequency of motion in the dynamic measurements, which leads to larger image interference in the video frame. However, the sensor's dynamic measurements are still highly consistent compared to the LVDT, and the maximum error rate of the peak dynamic strain measurement of the developed sensor is less than 1%, which meets the dynamic measurement requirements of common structures.

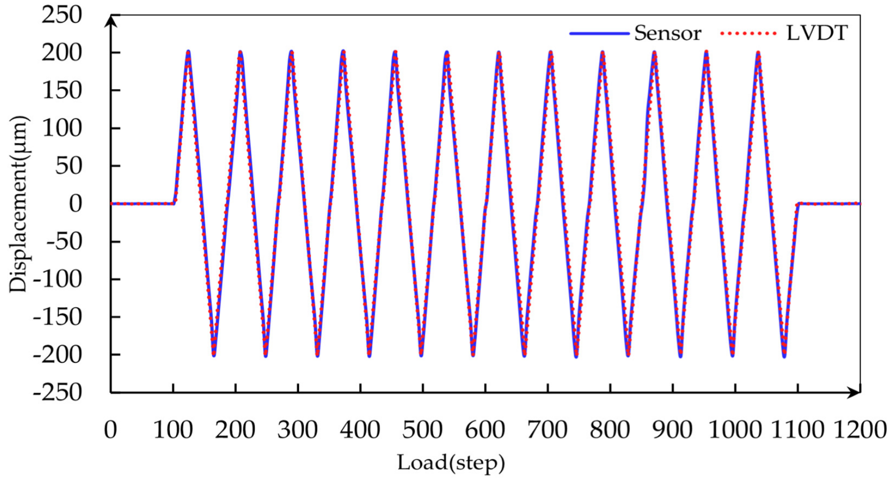

(**a**)

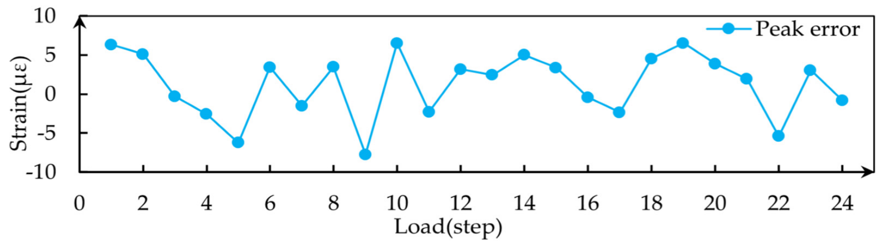

(**b**)

Figure 15. Resulting data and error data from the dynamic loading with LVDT comparison experiment: (**a**) comparison experiment data; (**b**) peak error data.

In summary, a series of experimental tests have fully proved that the newly developed slide-type strain sensor has a good measurement performance. The sensor has a small zero drift, a wide range, high repeatability, good accuracy, and can stably measure both static and dynamic strain responses. These results provide solid support for the application of this sensor in the field of structural health monitoring.

4. Actual Structure Measurement

After verifying the good performance of the sensor in the laboratory, we tested the performance of an assembled steel footbridge (Figure 16a) located in the dormitory area of the Dalian University of Technology for practical application. In order to ensure the feasibility and convenience of the measurement, based on the topography of the investigation, the target measurement section was finally set as the end span of the bridge (Figure 16b). Because the deformation of the bridge deck panel in the middle of the span is the largest, the measurement point was finally selected at the bottom of the bridge deck panel in the middle of the span, as shown in Figure 16c. Finally, the sensor was installed and fixed using a magnet and a strong adhesive, and the sensor after installation is shown in Figure 16d. Since the footbridge is mainly subjected to the dynamic load generated when pedestrians pass through, pedestrians stepping on the panel will lead to tensile strain at the bottom, so this test focuses on the dynamic measurement performance of the sensor at the same time. Considering that the purpose of this actual measurement is to validate the sensor's performance, we only continued to collect data for a few hours to validate.

(**a**)

(**b**)

(**c**)

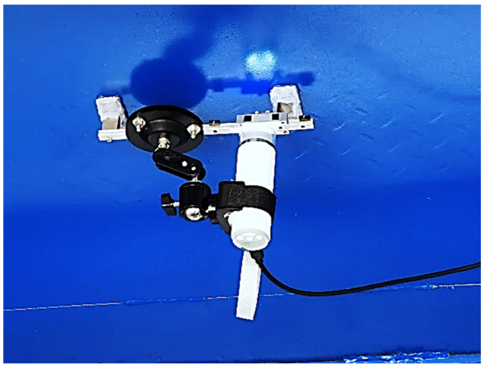

(**d**)

Figure 16. Schematic representation of the footbridge at the measurement point and physical demonstration of the sensor installation: (**a**) partial display of the footbridge in the monitoring section; (**b**) front view of target point; (**c**) elevation view of target measurement point; (**d**) physical drawing of the sensor after field installation.

4.1. Data Acquisition and Analysis

This measurement was started at noon on 7 July 2023, with a sensor measurement scale of 150 mm, and the acquisition method of a wired computer connection to the microscope was used to continuously monitor the measurement point for six hours through the mode of recording video, and the corresponding real-time monitoring results were obtained. Figure 17 demonstrates the data variation of the sensor in the initial state (switch not turned on) lasting about one minute. The curve in the figure demonstrates the magnitude of the zero drift of the sensor during the actual measurement, and eventually the strain fluctuation was found to be in the range of ±4 με, mainly concentrated in the range of ±2 με. Compared with the laboratory environment, the sensor data fluctuation in the actual measurement is slightly elevated due to the influence of the presence of temperature, pedestrian dynamic loads, and other factors on the sensor in the complex environment of the field. Nevertheless, the zero drift of the sensor in the actual measurement is still very small, which proves that the method still has good stability in the actual measurement.

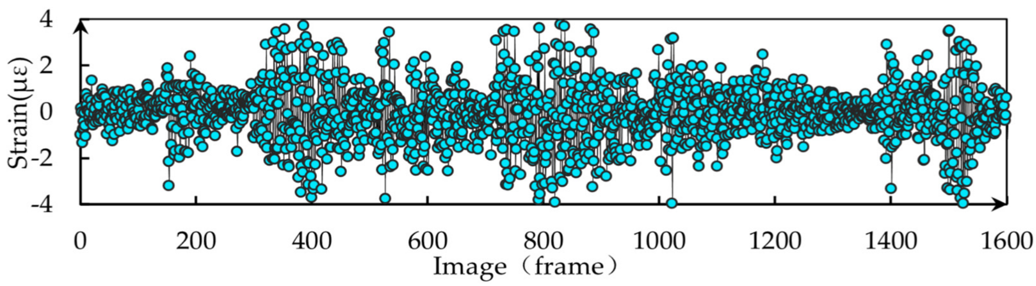

Figure 17. Zero drift data in the field for about one minute with the sensor switched off.

Figure 18 shows the strain real-time monitoring data at the measurement points taken from the monitoring process for two consecutive hours, from which it can be clearly observed that the developed sensors are able to accurately and in real time capture the strain changes at the measurement points of the bridge deck due to the dynamic loads generated by the pedestrians passing through. The figure shows that when there is no pedestrian passing the sensor data remain near the initial value and the strain curve remains horizontal. When there are pedestrians passing, the sensor can instantly capture the local strain changes at the bottom of the bridge deck caused by the dynamic load, and the strain curve fluctuates and peaks. The change rule of the monitoring data is consistent with the actual situation, the maximum strain on the surface of the measurement point is less than 400 με, and the dynamic measurement performance of the sensor has been tested in practical applications.

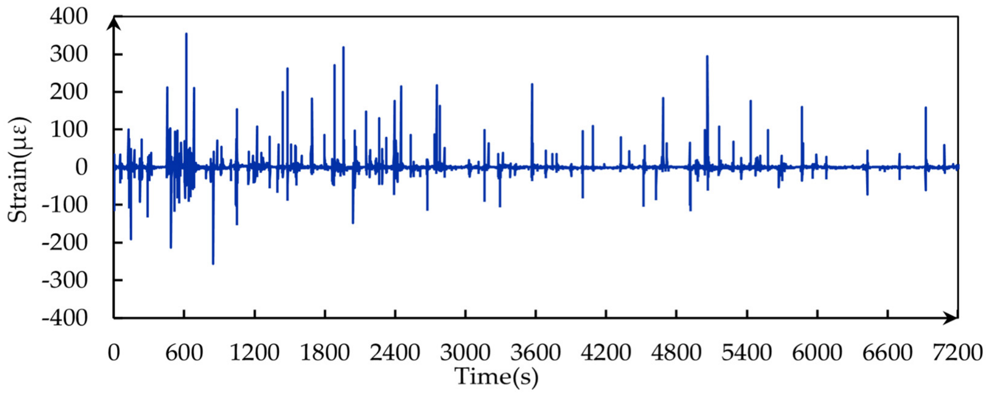

Figure 18. Real-time monitoring of strain data at structural measurement points by means of sensors (on-site time: 12.01–14.01).

4.2. Comparative Analysis with Pedestrian Traffic

The change in strain at the measurement point mainly comes from the dynamic load generated by the pedestrians passing through. Theoretically, the closer the moment when the strain curve measured by the sensor reaches the peak value and the moment when the pedestrians pass through the measurement point, the lower the hysteresis of the sensor in measuring the strain and the better the effect of the strain measurement. In order to verify the dynamic measurement performance of the sensor more comprehensively, we also set up monitoring equipment near the footbridge while the sensor was monitoring the strain. Two 10-minute-long recordings were made of the footage of pedestrians passing through the measurement point, and the start and end times were accurately recorded. Figure 19 shows the pedestrian passing at the measurement point in the filmed clip.

(**a**) (**b**)

Figure 19. Screenshots of pedestrians passing above the measurement point: (**a**) the first monitoring screenshot; (**b**) the second monitoring screenshot.

Then, the algorithm was used to recognize the two videos separately, and two curves of pedestrian flow over time were obtained, i.e., they reflect the change rule of the number of pedestrians passing over the measurement point over time, as shown by the red curve in Figure 20. When the curve is in a horizontal state, it indicates that no one passes the measurement point; when the curve begins to fluctuate upward, it indicates that there are pedestrians approaching the measurement point; when the curve reaches the peak, it is considered that there are pedestrians passing right above the measurement point at this time, and the peak of the curve represents the size of the flow of pedestrians passing through. In order to compare more intuitively, the two pedestrian flow change curves were placed in the corresponding time period of the sensor strain monitoring data, as shown in Figure 20, where the blue curve represents the strain monitoring data. It is worth mentioning that the actual significance of the vertical coordinates of the red curve in Figure 20 is ignored, and only the height of the peak and the moment of the peak are emphasized. The comparison shows that in the two extracted monitoring clips the moments at which the two curves reach their peaks are exactly the same, i.e., it means that the strain data monitored by the sensor reach their peak when the pedestrian passes right above the measurement point. The comparison is representative due to the random selection of the time of shooting the clips. The above results show that the sensors developed in this study can indeed capture the strain fluctuations caused by the dynamic load excitation due to pedestrians passing through the bridge deck in a timely manner. It further demonstrates that the sensor developed in this study has sufficient sensitivity for measurements on real structures with relatively low measurement hysteresis.

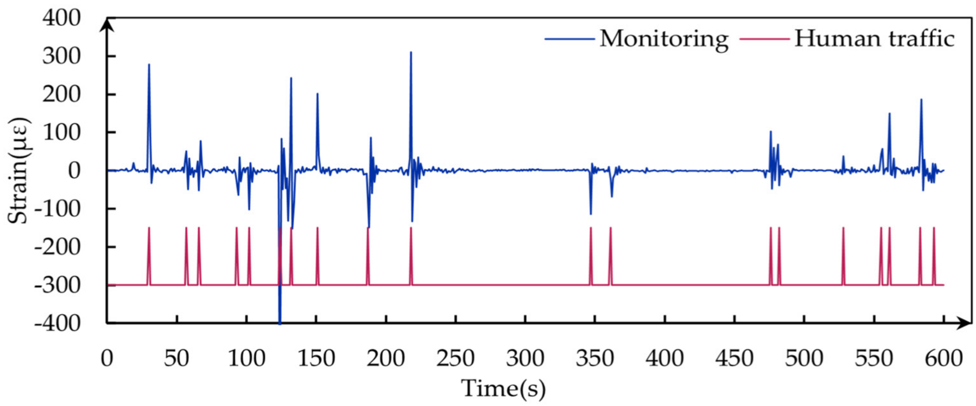

(**a**)

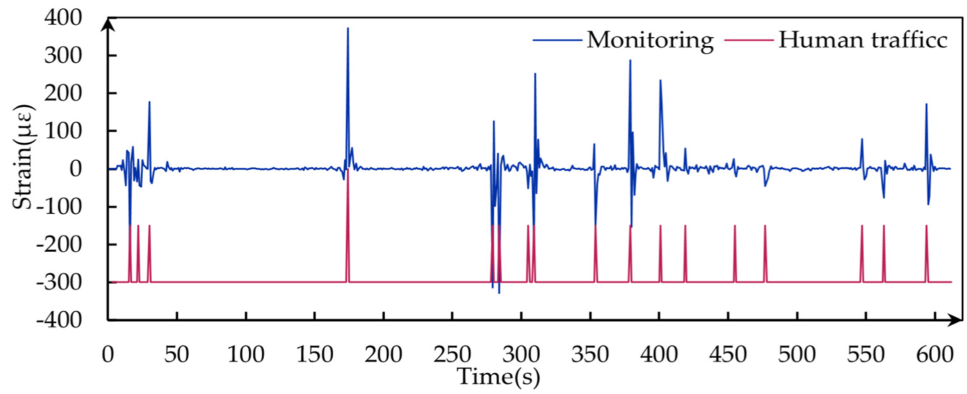

(**b**)

Figure 20. Comparison of strain data at the measurement points with data from the corresponding human flow excess change curves: (**a**) first monitoring segment; (**b**) second monitoring segment.

5. Conclusions

In this research, we have developed a strain measurement method based on template matching algorithms and microscopic vision techniques, designed and fabricated a sliding strain sensor, and selected a new multifunctional microscope that can be paired with a cell phone or a computer for strain measurement. The performance of the sensor has been tested in the laboratory, and the static and dynamic measurement capabilities of the sensor were verified by comparison with an LVDT. In addition, short-term field measurements on localized structures of pedestrian bridges have been completed to test the performance of the sensors in real-world applications. The conclusions are as follows:

(1) The sensors are made of stainless steel in accordance with a standardized process, making them more stable and durable. Among them, the new multifunctional microscope is chosen to effectively utilize the advantages of microscopic vision technology. Strain monitoring through a wired connection with a computer can ensure the stability of the sensor in long-term monitoring work. In particular, the sensor is equipped with the function of remote wireless acquisition by connecting with a cell phone, which makes the regular random inspection of structural strain more convenient and efficient.

(2) The sensor requires only simple installation and fixation for actual measurement. After successfully connecting with the cell phone or computer, strain measurement can be carried out, and the sensor does not need to be equipped with professional instruments. Therefore, the cost is relatively low, the operation is more convenient, even non-professionals can be quickly put into the strain measurement work, and the structure has universal applicability.

(3) In the laboratory performance test, the sensor shows good results: the zero drift is small, mainly concentrated in the range of ± 2 $\mu\varepsilon$ fluctuations; the effective tensile range is $\pm 19{,}745$ $\mu\varepsilon$, which can meet the range requirements of strain measurement in most engineering structures; and the standard deviation of the data with a single step repeated loading is only 0.456 $\mu\varepsilon$. In the comparison experiment with an LVDT, the maximum error of static loading is only 5 $\mu\varepsilon$, and the maximum error rate of dynamic loading is less than 1%, which proves that the sensor has high accuracy.

(4) In the measurement of the footbridge structure, the sensor is able to stably and effectively capture the strain changes on the surface of the structure, which shows a good dynamic measurement capability. Meanwhile, in the two randomly selected monitoring segments the time-dependent change curves of the pedestrian passage at the measurement points were exactly the same as the corresponding moments when the strain data reached the peak, which further proved that the sensors had sufficient sensitivity and relatively low hysteresis in the actual structural measurements.

In conclusion, the strain measurement system that has been developed in this study has the advantages of high accuracy, a low cost, convenient measurement, and wide applicability. It has been optimized for the problems of the current strain measurement means and provides a novel alternative means for strain measurement in the field of structural health monitoring, which is conducive to the promotion of large-scale universal structural strain measurement. However, under the complex environment in the field, the strain measurement is often interfered with by temperature, humidity, and other noise changes, which puts higher requirements on the service life of the sensor and anti-interference. In future work, it is necessary to further explore how to better reduce the impact of field noises on sensor measurements, and further optimization work for sensors will be of practical significance.

Author Contributions: Conceptualization, X.Z. and C.Z.; methodology, C.Z.; software, C.Z. and B.B.; validation, C.Z. and X.C.; investigation, L.L. and Z.C.; resources, L.L. and Z.C.; data curation, C.Z.; writing—original draft preparation, C.Z.; writing—review and editing, C.Z. and W.L.; supervision, X.Z. and W.L. All authors have read and agreed to the published version of the manuscript.

Funding: This study was funded by the National Natural Science Foundation of China (Grant No. 52378286).

Data Availability Statement: The authors acknowledge that data supporting the results of this study are available in the article. More detailed data can be obtained from the corresponding author, (X.Z.), upon reasonable request.

Conflicts of Interest: The authors declare no conflict of interest.

References

1. Balageas, D.; Fritzen, C.-P.; Güemes, A. *Structural Health Monitoring*; John Wiley & Sons: Hoboken, NJ, USA, 2010; ISBN 978-0-470-39440-3.
2. Comanducci, G.; Ubertini, F.; Materazzi, A.L. Structural Health Monitoring of Suspension Bridges with Features Affected by Changing Wind Speed. *J. Wind Eng. Ind. Aerodyn.* **2015**, *141*, 12–26. [CrossRef]
3. Payawal, J.M.G.; Kim, D.-K. Image-Based Structural Health Monitoring: A Systematic Review. *Appl. Sci.* **2023**, *13*, 968. [CrossRef]
4. Comisu, C.-C.; Taranu, N.; Boaca, G.; Scutaru, M.-C. Structural Health Monitoring System of Bridges. *Procedia Eng.* **2017**, *199*, 2054–2059. [CrossRef]
5. Sohn, H.; Farrar, C.R.; Hemez, F.M.; Czarnecki, J.J. *A Review of Structural Health Review of Structural Health Monitoring Literature 1996–2001*; Los Alamos National Lab. (LANL): Los Alamos, NM, USA, 2002.
6. Salawu, O.S. Detection of Structural Damage through Changes in Frequency: A Review. *Eng. Struct.* **1997**, *19*, 718–723. [CrossRef]
7. An, Y.; Chatzi, E.; Sim, S.-H.; Laflamme, S.; Blachowski, B.; Ou, J. Recent Progress and Future Trends on Damage Identification Methods for Bridge Structures. *Struct. Control Health Monit.* **2019**, *26*, e2416. [CrossRef]
8. Mashayekhi, M.; Santini-Bell, E. Three-Dimensional Multiscale Finite Element Models for in-Service Performance Assessment of Bridges. *Comput.-Aided Civ. Infrastruct. Eng.* **2019**, *34*, 385–401. [CrossRef]
9. Xu, Y.; Brownjohn, J.; Kong, D. A Non-Contact Vision-Based System for Multipoint Displacement Monitoring in a Cable-Stayed Footbridge. *Struct. Control Health Monit.* **2018**, *25*, e2155. [CrossRef]
10. Shrestha, A.; Dang, J.; Nakajima, K.; Wang, X. Image Processing–Based Real-Time Displacement Monitoring Methods Using Smart Devices. *Struct. Control Health Monit.* **2020**, *27*, e2473. [CrossRef]
11. Cavaco, E.; Pimenta, R.; Valença, J. A New Method for Corrosion Assessment of Reinforcing Bars Based on Close-Range Photogrammetry: Experimental Validation. *Struct. Concr.* **2019**, *20*, 996–1009. [CrossRef]
12. Dworakowski, Z.; Kohut, P.; Gallina, A.; Holak, K.; Uhl, T. Vision-Based Algorithms for Damage Detection and Localization in Structural Health Monitoring. *Struct. Control Health Monit.* **2016**, *23*, 35–50. [CrossRef]
13. Xu, J.; Dong, Y.; Zhang, Z.; Li, S.; He, S.; Li, H. Full Scale Strain Monitoring of a Suspension Bridge Using High Performance Distributed Fiber Optic Sensors. *Meas. Sci. Technol.* **2016**, *27*, 124017. [CrossRef]
14. Yan, W.-J.; Chronopoulos, D.; Cantero-Chinchilla, S.; Yuen, K.-V.; Papadimitriou, C. A Fast Bayesian Inference Scheme for Identification of Local Structural Properties of Layered Composites Based on Wave and Finite Element-Assisted Metamodeling Strategy and Ultrasound Measurements. *Mech. Syst. Signal Process.* **2020**, *143*, 106802. [CrossRef]
15. Scott, R.H.; Chikermane, S.; Vidakovic, M.; McKinley, B.; Sun, T.; Banerji, P.; Grattan, K.T.V. Development of Low Cost Packaged Fibre Optic Sensors for Use in Reinforced Concrete Structures. *Measurement* **2019**, *135*, 617–624. [CrossRef]
16. Cui, H.; Du, H.; Zhao, F.; Hong, M. Damage Identification in a Plate Structure Based on a Cross-Direction Strain Measurement Method. *Measurement* **2020**, *158*, 107714. [CrossRef]
17. Sierra-Pérez, J.; Güemes, A.; Mujica, L.E. Damage Detection by Using FBGs and Strain Field Pattern Recognition Techniques. *Smart Mater. Struct.* **2012**, *22*, 025011. [CrossRef]
18. Li, J.; Hao, H.; Fan, K.; Brownjohn, J. Development and Application of a Relative Displacement Sensor for Structural Health Monitoring of Composite Bridges. *Struct. Control Health Monit.* **2015**, *22*, 726–742. [CrossRef]
19. dos Reis, J.; Costa, C.O.; da Costa, J.S. Local Validation of Structural Health Monitoring Strain Measurements. *Measurement* **2019**, *136*, 143–153. [CrossRef]
20. Hu, X.; Wang, B.; Ji, H. A Wireless Sensor Network-Based Structural Health Monitoring System for Highway Bridges. *Comput.-Aided Civ. Infrastruct. Eng.* **2013**, *28*, 193–209. [CrossRef]
21. Das, S.; Saha, P. A Review of Some Advanced Sensors Used for Health Diagnosis of Civil Engineering Structures. *Measurement* **2018**, *129*, 68–90. [CrossRef]
22. Zhang, L.; Qiu, G.; Chen, Z. Structural Health Monitoring Methods of Cables in Cable-Stayed Bridge: A Review. *Measurement* **2021**, *168*, 108343. [CrossRef]
23. dos Reis, J.; Costa, C.O.; da Costa, J.S. Strain Gauges Debonding Fault Detection for Structural Health Monitoring. *Struct. Control Health Monit.* **2018**, *25*, e2264. [CrossRef]
24. Kahandawa, G.C.; Epaarachchi, J.; Wang, H.; Lau, K.T. Use of FBG Sensors for SHM in Aerospace Structures. *Photonic Sens.* **2012**, *2*, 203–214. [CrossRef]
25. Lee, H.M.; Choi, S.W.; Jung, D.; Park, H.S. Analytical Model for Estimation of Maximum Normal Stress in Steel Beam-Columns Based on Wireless Measurement of Average Strains from Vibrating Wire Strain Gages. *Comput.-Aided Civ. Infrastruct. Eng.* **2013**, *28*, 707–717. [CrossRef]

26. Marques, F.; Moutinho, C.; Magalhães, F.; Caetano, E.; Cunha, Á. Analysis of Dynamic and Fatigue Effects in an Old Metallic Riveted Bridge. *J. Constr. Steel Res.* **2014**, *99*, 85–101. [CrossRef]
27. Azarbayejani, M.; Jalalpour, M.; El-Osery, A.I.; Taha, M.M.R. Field Application of Smart SHM Using Field Programmable Gate Array Technology to Monitor an RC Bridge in New Mexico. *Smart Mater. Struct.* **2011**, *20*, 085005. [CrossRef]
28. Ni, Y.Q.; Chen, R. Strain Monitoring Based Bridge Reliability Assessment Using Parametric Bayesian Mixture Model. *Eng. Struct.* **2021**, *226*, 111406. [CrossRef]
29. Tondini, N.; Bursi, O.S.; Bonelli, A.; Fassin, M. Capabilities of a Fiber Bragg Grating Sensor System to Monitor the Inelastic Response of Concrete Sections in New Tunnel Linings Subjected to Earthquake Loading. *Comput.-Aided Civ. Infrastruct. Eng.* **2015**, *30*, 636–653. [CrossRef]
30. Zhu, H.; Gao, K.; Xia, Y.; Gao, F.; Weng, S.; Sun, Y.; Hu, Q. Multi-Rate Data Fusion for Dynamic Displacement Measurement of Beam-like Supertall Structures Using Acceleration and Strain Sensors. *Struct. Health Monit.* **2020**, *19*, 520–536. [CrossRef]
31. Xia, Y.; Ni, Y.; Zhang, P.; Liao, W.; Ko, J. Stress Development of a Supertall Structure during Construction: Field Monitoring and Numerical Analysis. *Comput.-Aided Civ. Infrastruct. Eng.* **2011**, *26*, 542–559. [CrossRef]
32. Vazquez-Ontiveros, J.R.; Vazquez-Becerra, G.E.; Quintana, J.A.; Carrion, F.J.; Guzman-Acevedo, G.M.; Gaxiola-Camacho, J.R. Implementation of PPP-GNSS Measurement Technology in the Probabilistic SHM of Bridge Structures. *Measurement* **2021**, *173*, 108677. [CrossRef]
33. Fernández-Medina, A.; Frövel, M.; Heredero, R.L.; Belenguer, T.; de la Torre, A.; Moravec, C.; Julián, R.S.; Gonzalo, A.; Cebollero, M.; Álvarez-Herrero, A. Embedded Fiber Bragg Grating Sensors for Monitoring Temperature and Thermo-Elastic Deformations in a Carbon Fiber Optical Bench. *Sensors* **2023**, *23*, 6499. [CrossRef] [PubMed]
34. Bertulessi, M.; Bignami, D.F.; Boschini, I.; Longoni, M.; Menduni, G.; Morosi, J. Experimental Investigations of Distributed Fiber Optic Sensors for Water Pipeline Monitoring. *Sensors* **2023**, *23*, 6205. [CrossRef] [PubMed]
35. Lou, Y.; Yang, T.; Luo, D.; Wu, J.; Dong, Y. A Novel Catheter Distal Contact Force Sensing for Cardiac Ablation Based on Fiber Bragg Grating with Temperature Compensation. *Sensors* **2023**, *23*, 2866. [CrossRef]
36. Wang, Y.; Hoult, N.A.; Woods, J.E.; Kassenaar, H.; Bao, X. Distributed Impact Wave Detection in Steel I-Beam with a Weak Fiber Bragg Gratings Array. *Sensors* **2023**, *23*, 2194. [CrossRef] [PubMed]
37. Tan, X.; Abu-Obeidah, A.; Bao, Y.; Nassif, H.; Nasreddine, W. Measurement and Visualization of Strains and Cracks in CFRP Post-Tensioned Fiber Reinforced Concrete Beams Using Distributed Fiber Optic Sensors. *Autom. Constr.* **2021**, *124*, 103604. [CrossRef]
38. Pan, B.; Qian, K.; Xie, H.; Asundi, A. Two-Dimensional Digital Image Correlation for in-Plane Displacement and Strain Measurement: A Review. *Meas. Sci. Technol.* **2009**, *20*, 062001. [CrossRef]
39. Pan, B.; Yu, L.; Zhang, Q. Review of Single-Camera Stereo-Digital Image Correlation Techniques for Full-Field 3D Shape and Deformation Measurement. *Sci. China Technol. Sci.* **2018**, *61*, 2–20. [CrossRef]
40. Luo, L.; Feng, M.Q.; Wu, J.; Bi, L. A Vision-Based Surface Displacement/Strain Measurement Technique Based on Robust Edge-Enhanced Transform and Algorithms for High Spatial Resolution. *Struct. Control Health Monit.* **2021**, *28*, e2797. [CrossRef]
41. Gopalakrishnan, K.; Khaitan, S.K.; Choudhary, A.; Agrawal, A. Deep Convolutional Neural Networks with Transfer Learning for Computer Vision-Based Data-Driven Pavement Distress Detection. *Constr. Build. Mater.* **2017**, *157*, 322–330. [CrossRef]
42. Feng, D.; Feng, M.Q. Computer Vision for SHM of Civil Infrastructure: From Dynamic Response Measurement to Damage Detection—A Review. *Eng. Struct.* **2018**, *156*, 105–117. [CrossRef]
43. Chen, J.G.; Davis, A.; Wadhwa, N.; Durand, F.; Freeman, W.T.; Büyüköztürk, O. Video Camera–Based Vibration Measurement for Civil Infrastructure Applications. *J. Infrastruct. Syst.* **2017**, *23*, B4016013. [CrossRef]
44. Zhang, L.; Liu, P.; Yan, X.; Zhao, X. Middle Displacement Monitoring of Medium–Small Span Bridges Based on Laser Technology. *Struct. Control Health Monit.* **2020**, *27*, e2509. [CrossRef]
45. Hang, Y.; Liu, P.; Zhao, X. Structural Displacement Monitoring Based on Mask Regions with Convolutional Neural Network. *Constr. Build. Mater.* **2021**, *267*, 120923. [CrossRef]
46. Chen, P.-H.C.; Gadepalli, K.; MacDonald, R.; Liu, Y.; Kadowaki, S.; Nagpal, K.; Kohlberger, T.; Dean, J.; Corrado, G.S.; Hipp, J.D.; et al. An Augmented Reality Microscope with Real-Time Artificial Intelligence Integration for Cancer Diagnosis. *Nat. Med.* **2019**, *25*, 1453–1457. [CrossRef]
47. Wang, W.; Coop, M.R. An Investigation of Breakage Behaviour of Single Sand Particles Using a High-Speed Microscope Camera. *Geotechnique* **2016**, *66*, 984–998. [CrossRef]
48. Xie, B.; Chen, X.; Ding, M.; Zhou, G.; Zhao, X. Design and Development of a New Strain Measuring Method Based on Smartphone and Machine Vision. *Measurement* **2021**, *182*, 109724. [CrossRef]
49. Xie, B.; Li, J.; Zhao, X. Strain Measurement Based on Speeded-up Robust Feature Algorithm Applied to Microimages from a Smartphone-Based Microscope. *Sensors* **2020**, *20*, 2805. [CrossRef]
50. Xie, B.; Li, J.; Zhao, X. Accuracy and Sensibility Analysis of Strain Measurement Based on Microimages Captured by Smartphone with a Microscope. *Struct. Control. Health Monit.* **2021**, *28*, e2692. [CrossRef]
51. Xie, B.; Zhang, L.; Ding, M.; Li, W.; Zhao, X. Strain Measurement Based on Cooperative Operation with Different Smartphones. *Comput.-Aided Civ. Infrastruct. Eng.* **2023**, *38*, 241–252. [CrossRef]
52. Zhang, L.; Xie, B.; Li, W.; Zhou, G.; Zhao, X. Design and Initial Validation of Micro Image Strain Sensing System Based on Digital Microscope-Camera. *Opt. Laser Technol.* **2022**, *149*, 107858. [CrossRef]

53. Akinlar, C.; Topal, C. EDCircles: A Real-Time Circle Detector with a False Detection Control. *Pattern Recognit.* **2013**, *46*, 725–740. [CrossRef]
54. Omachi, S.; Omachi, M. Fast Template Matching with Polynomials. *IEEE Trans. Image Process.* **2007**, *16*, 2139–2149. [CrossRef] [PubMed]
55. Liu, X.; Li, Y.; Guo, Y.; Zhou, L. Printing Defect Detection Based on Scale-Adaptive Template Matching and Image Alignment. *Sensors* **2023**, *23*, 4414. [CrossRef]
56. Lee, S.; Kim, S.-W. Recognition of Targets in SAR Images Based on a WVV Feature Using a Subset of Scattering Centers. *Sensors* **2022**, *22*, 8528. [CrossRef] [PubMed]
57. Centracchio, J.; Parlato, S.; Esposito, D.; Bifulco, P.; Andreozzi, E. ECG-Free Heartbeat Detection in Seismocardiography Signals via Template Matching. *Sensors* **2023**, *23*, 4684. [CrossRef] [PubMed]
58. Han, Y. Reliable Template Matching for Image Detection in Vision Sensor Systems. *Sensors* **2021**, *21*, 8176. [CrossRef] [PubMed]
59. Mukhopadhyay, P.; Chaudhuri, B.B. A Survey of Hough Transform. *Pattern Recognit.* **2015**, *48*, 993–1010. [CrossRef]
60. Cha, J.; Cofer, R.H.; Kozaitis, S.P. Extended Hough Transform for Linear Feature Detection. *Pattern Recognit.* **2006**, *39*, 1034–1043. [CrossRef]
61. Ou, Y.; Deng, H.; Liu, Y.; Zhang, Z.; Lan, X. An Anti-Noise Fast Circle Detection Method Using Five-Quadrant Segmentation. *Sensors* **2023**, *23*, 2732. [CrossRef]
62. Ou, Y.; Deng, H.; Liu, Y.; Zhang, Z.; Ruan, X.; Xu, Q.; Peng, C. A Fast Circle Detection Algorithm Based on Information Compression. *Sensors* **2022**, *22*, 7267. [CrossRef]